Author(s): Mattos, Bruno D.; Jäntti, Noora; Khakalo, Sergei; Zhu, Ya; Miettinen, Arttu; Parkkonen, Joni; Khakalo, Alexey; Rojas, Orlando J.; Ago, Mariko

Title: Black Bioinks from Superstructured Carbonized Lignin Particles

Year: 2023

Version: Published version

Please cite the original version:

Mattos, B. D., Jäntti, N., Khakalo, S., Zhu, Y., Miettinen, A., Parkkonen, J., Khakalo, A., Rojas, O. J., & Ago, M. (2023). Black Bioinks from Superstructured Carbonized Lignin Particles. Advanced Functional Materials, 33(45), Article 2304867. https://doi.org/10.1002/adfm.202304867

ADVANCED FUNCTIONAL MATERIALS
www.afm-journal.de

Black Bioinks from Superstructured Carbonized Lignin Particles

Bruno D. Mattos, Noora Jäntti, Sergei Khakalo, Ya Zhu, Arttu Miettinen, Joni Parkkonen, Alexey Khakalo, Orlando J. Rojas,* and Mariko Ago**

A renewable source of carbon black is introduced by the processing of lignin from agro-forestry residues. Lignin side streams are converted into spherical particles by direct aerosolization followed by carbonization. The obtained submicron black carbon is combined with cellulose nanofibers, which act as a binder and rheology modifier, resulting in a new type of colloidal bioink. The bioinks are tested in handwriting and direct ink writing. After consolidation, the black bioinks display total light reflectance (%R) at least three times lower than commercial black inks (reduction from 12 to 4%R). A loading of up to 20% of nanofibers positively affects the cohesion of the dried bioink (1 to 16 MPa), with no significant reduction in light reflectance. This is a result of the superstructuring of the ink components, which disrupts particle packing, intensifies colloidal interactions, introduces light absorption, and non-reflective multiple scattering.

1. Introduction

Black substances are used in a broad range of applications, from textile dyeing to energy harvesting. For instance, black inks are by far the most used for printing and writing since it provides the highest contrast with common white substrates (paper, cotton, etc). Black substances comprise chemical components that change their energetic state by absorbing light energy with wavelengths (WL) in the visible range (380–700 nm). Conjugated polyaromatics, including those derived from carbonized biomass, exhibit short optical bandgap (*ca.* 1–1.5 eV) enabling *HOMO*-to-*LUMO* transitions by absorbing low-energy photons, such as those in the visible electromagnetic spectrum.[1,2] Commonly used black pigments are sourced from petroleum-based coal and oil, animal bones, and iron oxides.[3,4] Yet, a vast amount of waste biomass rich in polyphenols[5] can be transformed into condensed graphitic structures upon carbonization,[6] opening an opportunity for alternative biobased pigments.

The most efficient carbon-based pigments absorb only ≈90% of the incident light. This is because of a defective polyaromatic structure that decreases the absorption efficiency, thus promoting significant light reflectance. The black color from pigments is primarily associated with their molecular structure, which can be optimized to reduce light reflection, e.g., by introducing structural features on their surface. Some geometries can induce multiple internal reflections that trap light and limit reflection.[7–11] Several designs have been proposed to decrease light reflectivity, including thin-films or arrays of vertically aligned carbon nanotubes (CNT),[11] carbonized low-density

B. D. Mattos, N. Jäntti, Y. Zhu, O. J. Rojas
Department of Bioproducts and Biosystems
School of Chemical Engineering
Aalto University
Vuorimiehentie 1, Espoo FI-00076, Finland
E-mail: bruno.mattos@aalto.fi; orlando.rojas@aalto.fi

S. Khakalo
Department of Civil Engineering
School of Engineering
Aalto University
Rakentajanaukio 4, Espoo FI-00076, Finland

S. Khakalo
Integrated Computational Materials Engineering
VTT Technical Research Centre of Finland Ltd.
Vuorimiehentie 2, Espoo FI-02044, Finland

A. Miettinen, J. Parkkonen
Department of Physics
University of Jyvaskyla
Survontie 9, Jyväskylä FI-40014, Finland

A. Khakalo
Cellulose Coatings and Films
VTT Technical Research Centre of Finland Ltd.
Tietotie 4E, Espoo FI-02044, Finland

O. J. Rojas
Bioproducts Institute
Department of Chemical and Biological Engineering
Department of Chemistry and Department of Wood Science
University of British Columbia
Vancouver, British Columbia V6T 1Z4, Canada

M. Ago
Institute of Agriculture
Tokyo University of Agriculture and Technology
3-5-8, Saiwai, Fuchu, Tokyo 183-8509, Japan
E-mail: marikoago@go.tuat.ac.jp

The ORCID identification number(s) for the author(s) of this article can be found under https://doi.org/10.1002/adfm.202304867

DOI: 10.1002/adfm.202304867

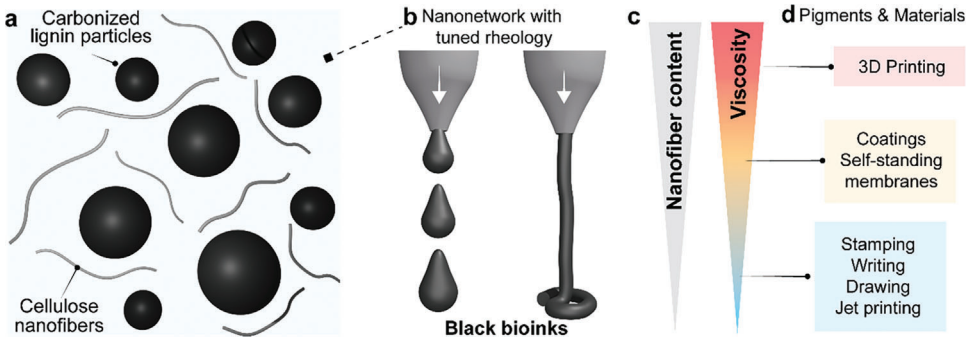

Figure 1. Aqueous suspensions of light-interacting plant biocolloids are used to prepare versatile black bioinks. a) Carbonized lignin particles are used as light absorbing components, whereas cellulose nanofibers assemble into partially visibly transparent structures are used as colloidal binders. b) The combination of both plant biocolloids enables nanostructures with tuned rheology, with c) viscosity increasing with the increase of nanofiber content. d) The various formulations enable a wide variety of applications for these precursors, from various pigmentation methods to several techniques used for materials assembly.

wood,[12] and polymer-based carbon aerogels.[7] CNT technologies are highly dependent on a metallic substrate for their growth into an array by chemical vapor deposition, whereas carbonized wood and aerogels are mechanically weak.

Particle-fiber nanonetworks can yield solid constructs that develop nanoscale structural features upon consolidation from aqueous colloidal suspensions.[13] Moreover, particle-nanofiber constructs can be engineered to maximize the cohesiveness and to induce light entrapment. In fact, we propose that such colloidal (black) inks can be made completely from plant-based building blocks, namely cellulose nanofibers, and lignin particles. Spherical lignin particles[14] can be carbonized to yield submicron black particles that evolve into a graphitic chemical structure upon pyrolysis. Constructs made only of submicron particles are brittle and depending on the consolidation conditions, they tend to self-organize into ordered lattices that can display photonic colors.[15] Superstructuring particles with cellulose nanofibers (CNF), however, disrupts the particle packing and creates an irregular and porous particle network. Herein, CNF is proposed as an alternative to current binders, for instance those based on epoxy or acrylics that yield glossy and/or greyish colors. CNF introduces cohesion by the formation of an interconnected particle-nanofiber entangled network.[13,16] This is a result of early gelation of CNF suspensions, which reduces particle mobility and prevents densification. The length scales of CNF assemblies around submicron particles is below the visible wavelength range,[13] which minimizes light scattering and reflection. The latter makes CNF an ideal binder for particles intended for photonic applications within the visible WL (CNF is considered transparent in these assemblies and does not hinder the access of light energy to the superstructured particles). This is highly relevant to the preparation of black inks as the addition of a binding component should not impact their blackness.

We introduce a versatile black bioink by combining light-absorbing particles obtained from lignin and CNF-based transparent structural binders (**Figure 1**a). Consolidation of the black bioinks results in superstructured particle-nanofiber networks that couple chemical (i.e., gaphitic structures) and structural (i.e., porosity) features that achieve low light reflectance. Application of CNF as a structural binder enables an additional control over the ink viscosity and flow behavior (Figure 1b,c), thus allowing uses in a wide range of applications (Figure 1d). In fact, CNF has been extensively used as rheology modifier in the development of various ink formulations.[17–20] We demonstrate the versatility of the black bioinks in coatings, writing, and 3D printing, but we envision these pigments in ink-jet printing, stamping, and painting. We provide further insights on the effects of composition and drying conitions by assessing the optical properties of black bioinks in the framework of finite element modeling.

2. Results and Discussion

2.1. Plant-Based Black Pigments

Lignosulfonate powder (LS), as obtained from industry, is an irregular particulate given the uncontrolled drying conditions from a typically concentrated solution. Direct carbonization of such precursor yields, non-differently, irregular particles with sizes ranging from 20 to 200 µm (**Figure 2**a). Spherical lignin particles with diameter *ca.* 1.5 µm (Figure 2b) were prepared using an aerosol reactor. In this process, lignin solutions are prepared at low concentration, and then atomized into small droplets that are slowly dried under a N_2 flow.[14,21] After this the lignin particles were thermally treated at 170 °C and then carbonized at temperatures ranging from 600 to 900 ^{0}C under N_2 atmosphere. The carbonized lignin particles (cLSP) shrunk by *ca.* 30% during carbonization, leading to particles ranging from 900 nm to 1 µm in diameter (Figure 2c,d and Figure S1, Supporting Information). Carbonized lignosulfonate powder (cLS) and particles (cLSP) are chemically equivalent (see similar Raman profiles in Figure 2e,f). The signals in the Raman spectra refer to first-order defect-induced D band at ≈1350 cm^{-1} (breathing mode of A_{1g} symmetry), and G band at ≈1580 cm^{-1} (in-plane bond stretching motion of sp^2 carbon atoms of E_{2g} symmetry).[1] The ratio between these two bands, namely D/G ratio, as well as their peak position and shape (full width at half maximum, FWHM) are used to locate the obtained carbons within the structural scale for carbon, i.e., from (hydrogenated) disordered graphite to tetrahedral amorphous carbon (*ta*-C, diamond-like carbon). Following the three-stage model proposed by Ferrari and Robertson,[1] describing the amorphization trajectory ranging from graphite to *ta*-C, our cLS and cLSP comprise semi-nanocrystalline carbon

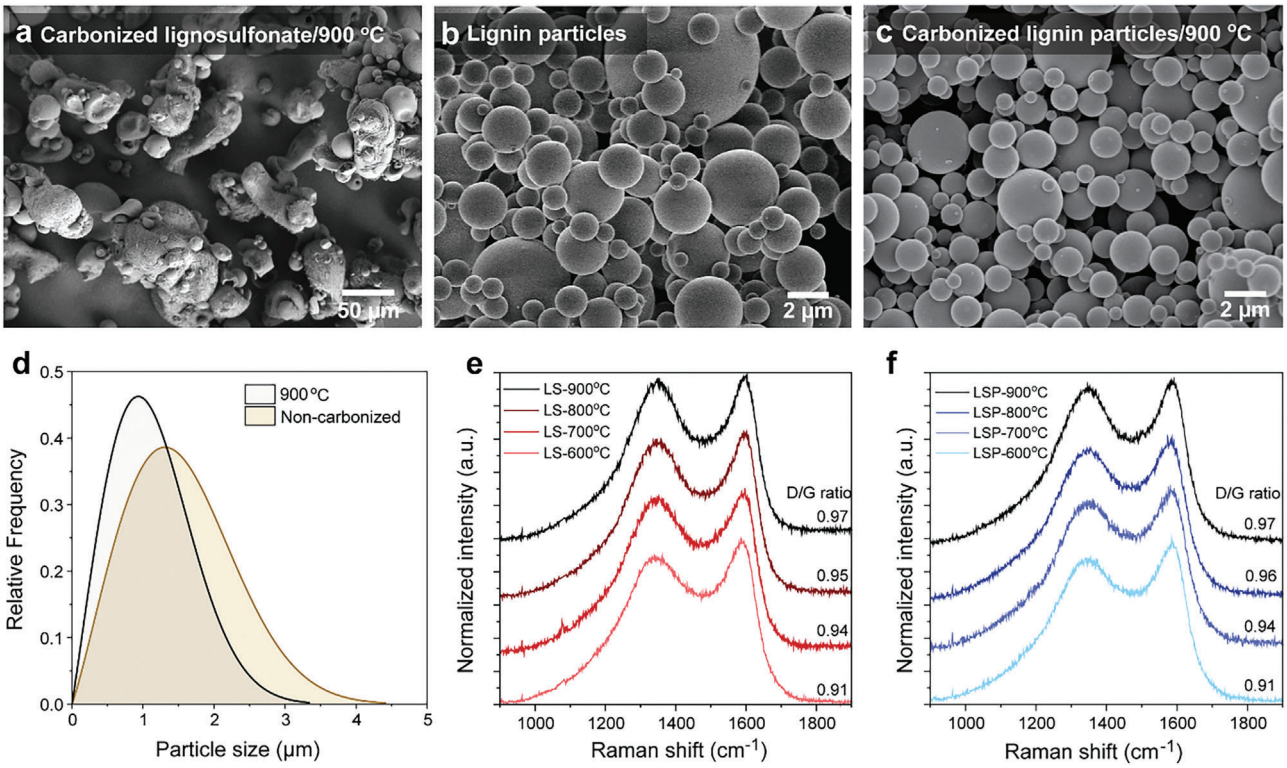

Figure 2. Structural properties of the carbonized lignin materials. Scanning electron microscope images of a) carbonized lignosulfonate powder (cLS), b) lignin particles (LSP) used as precursors for obtaining c) carbonized lignin particles (cLSP). d) Size distribution of lignin particles before and after carbonization at 900 °C, showing a decrease in particle size after thermal treatment. Raman spectra of e) lignosulfonate (cLS) and f) lignin particles (cLSP) carbonized at temperatures ranging from 600 to 900 °C. Respective D/G ratio is shown next to each spectrum.

structures with slightly increased cluster sizes as the temperature of carbonization goes from 600 to 900 ^{0}C. Nonetheless, although the D/G ratio increases with the carbonization temperature, the range of values are rather narrow (from 0.91 to 0.97) and the wide FWHM remains nearly constant (*ca.* 100 cm^{-1} for D band and *ca.* 60 cm^{-1} for G band), so that all samples display nearly the same nanocrystalline graphitic structure (Table S1, Supporting Information). This corroborates previous work on the carbonization of ligneous biomass, where distinguishable changes on the carbon structure are seen only after 1400 ^{0}C.[6] Semi-nanocrystalline carbons, with D/G ≈1, display optical bandgap (*HOMO-LUMO* gap) ranging from 1 to 1.5 eV approximatively,[1,2] falling below the visible light energies (1.8–3.1 eV). Therefore, carbons obtained either from synthetic precursors or biomass are naturally black as their chemical structure enables the *HOMO* to *LUMO* transition to take place by absorbing (low) energy within the visible range.

2.2. Lignin-CNF Colloidal Black Bioinks

In our lignin-based black pigments, the chemistry-derived blackness inherent to cLS and cLSP is the same. However, when using these black pigments as bioinks for coatings or structured materials, the total light reflectance of the dried phase depends on the structure, which in turn depends on the a) dimensions and morphology of the particles, b) the binder, and the c) binder-pigment structuring. Particle superstructuring with CNF disrupts the particle packing, thus creating an irregular and porous particle-fiber network that induce multiple internal light reflections. Moreover, addition of loadings as low as 0.1 wt.% of CNF improves the colloidal stability of carbon particles suspensions (Figure S2, Supporting Information), via electrostatic interactions[22] and by creating interpenetrated fibrillar nanonetworks.[13]

The consolidation of the black bioinks yielded materials with varied morphologies from the macro to the nanoscale, which depended on the black pigment used. First, we used X-ray tomography (at either 1.15 µm or 65 nm of resolution) to investigate the macroscopic features (**Figure 3**) of the dried phases of the cLS and cLSP based bioinks, both using CNF at 10 wt.% as binder (note: the effect of content and type of binder on the properties of the materials is shown later). The 3D visualizations in Figure 3a,b indicate that both bioinks resulted in homogenous materials with no phase separation observed at the macroscale. Only a few aggregates were found in the cLSP construct (Figure 3c). 2D slices of the tomograms confirm the low packing degree and the homogenous distribution of the cLS powder and cLSP within the nanocellulose binder (Figure S3, Supporting Information). The roughness of the top surface varied depending on the black pigment used, which is observed in the color maps for surface height (Figure 3d). Overall, bigger pigments led to a wider minima–maxima height span both at the top (drying front) and bottom (in contact with the underlying substrate during drying) surfaces of the materials (Figure 3d and Figure S4, Supporting

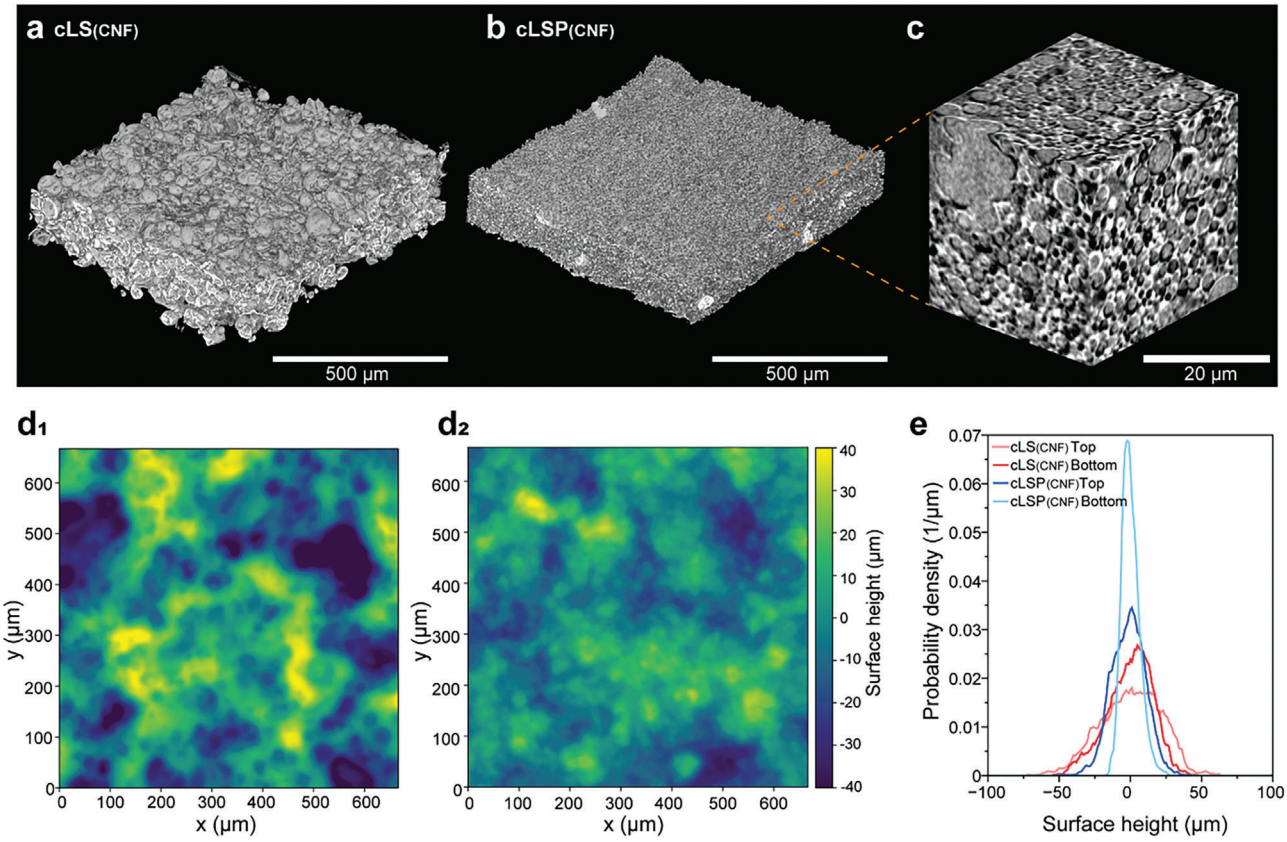

Figure 3. Macroscopic morphology of the dried bioinks. 3D visualization, built from microCT scans, of a) cLS(CNF) and b) cLSP(CNF) materials. c) 3D visualization of cLSP(CNF) built from nanoCT scans with a pixel size of 65 nm. Color maps for surface height variations at the top surface of d_1) cLS(CNF) and d_2) cLSP(CNF) materials. e) Numerical results for surface height of the top and bottom surfaces of the cLS(CNF) and cLSP(CNF) materials. Note: 3D visualizations contain perspective and might induce minor deviations in the accuracy of the scale bars. We used orthographic projection to minimize such deviations.

Information). In terms of surface height, the cLS materials had a much larger dimensional span of 100 µm compared to the cLSP, which was one order of magnitude lower (*ca.* 10 µm) (Figure 3e).

Although rougher at the macroscale, the cLS materials are microscopically smoother than those materials constructed with cLSP. The size range of the cLS pigments varies from 20 to 200 µm, which can characterize a flat-like surface depending on the length scale. This is especially relevant in the context of visible light absorption, whose wavelength are below 1 µm. On the other hand, materials comprising a given concentration of cLSP and varying amounts of CNF, yielded superstructured particle constructs with submicron geometrical features (**Figure 4**a). The latter lower the light reflectance by favoring light reflection inward, within the structure, resulting in light trapping and near-complete absorption. These features are absent in cLS/CNF bioinks, given the size of the cLS pigments (one order of magnitude larger than that of cLSP, Figure 4a1,a2). The drastically different morphologies of the dried inks (Figure 4a) impact the cohesion of the particle-CNF network, depending mostly on content and type of binder. We investigated the efficiency of nanocellulose binders in bringing cohesion to the light-absorbing particles by using TEMPO (2,2,6,6-tetramethylpiperidine-1-oxyl radical)-oxidized (TOCNF) and unmodified cellulose nanofibers (CNF). To assess the strength of the dried bioink, we prepared macroscopic cylinders using templated evaporation induced self-assembly of cLSP/cLS mixed with either TOCNF or CNF. The dried cylinders were then subjected to uniaxial compression and their stress at the yield point was compared (Figure 4b—inset). In detail, the yield point refers to transition between elastic and plastic deformation, whereby particle-nanofiber networks experience crack generation and propagation. Crack propagation is rather limited in CNF-particle constructs due to the interconnectivity of the network, thus leading to a plateau in the stress–strain curve where small fractures took place but were held together by the nanofibers.[16]

Overall, the size of the particle dictates the topology of the nanofiber network, which has an impact on the cohesion of the material.[13] The nanocellulose binder assembled into a paper-like structure around the particles (20–200 µm in size), whereas it created an intermixed 3D particle-nanofiber network with cLSP of 900 nm. The utilization of spherical cLSP led to particle-nanofiber networks two times more cohesive than those obtained by irregular cLS, which is more accentuated when using >9 wt.% binder (Figure 4b). CNF networks are more effective to reduce cracking in assemblies of submicron particles, when compared with bigger (>40 µm) particle counterparts (Figure S5, Supporting Information). The stress at yield point increases in a *quasi*-linear fashion with the binder content. The highest strength for

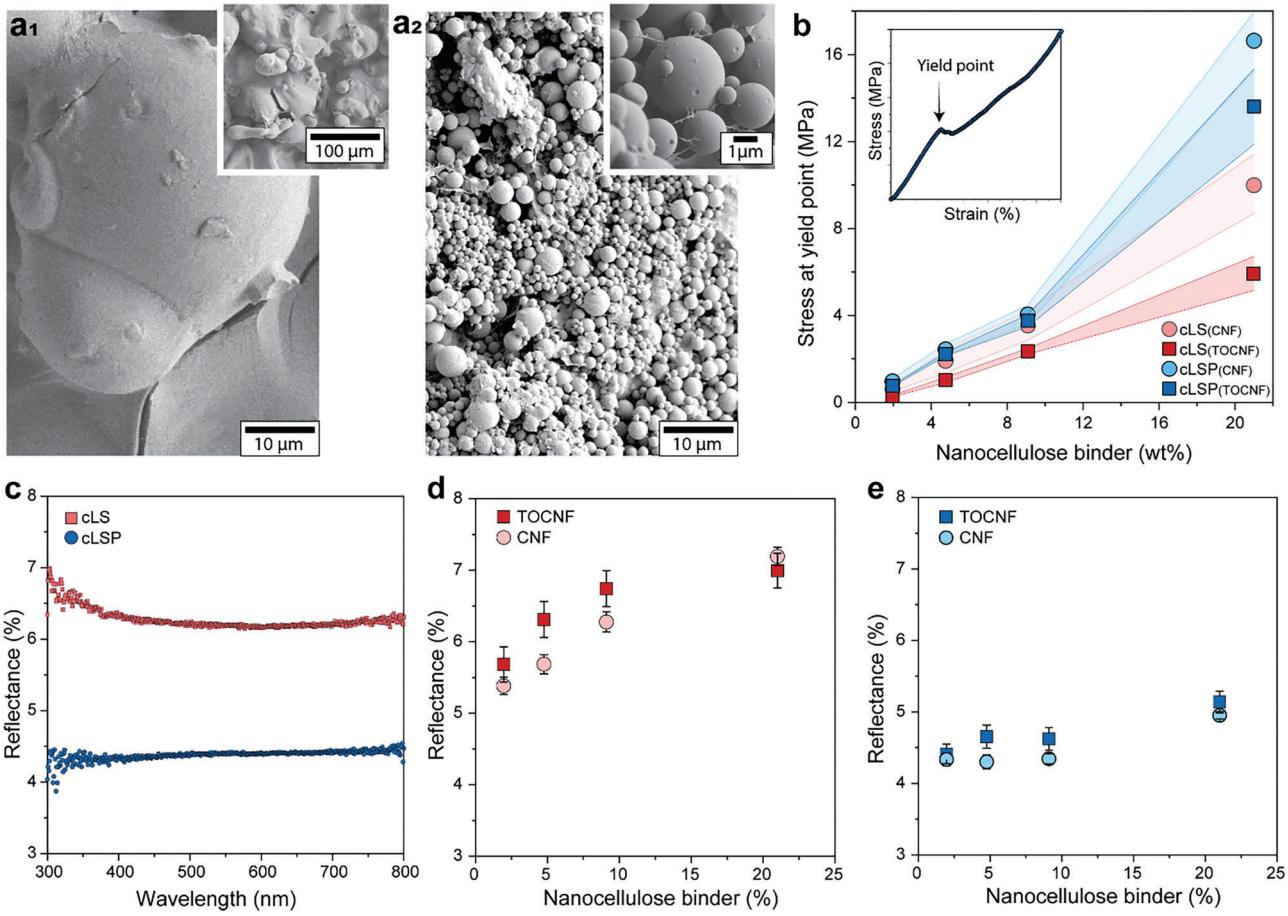

Figure 4. Cohesion and light reflectance properties of ink precursors consolidated into particle-nanofiber macroscopic constructs. Scanning electron microscope images of a_1) cLS and a_2) cLSP membranes assembled using 9 wt.% of CNF. b) Stress at yield point as a function of binder content and type, as well as particle type (inset graph show the yield point). c) UV–visible spectra obtained in reflectance mode of cLS and cLSP membranes assembled with 9 wt.% CNF content. Averaged reflectance (300–800 nm) of d) cLS and e) cLSP membranes consolidated with TOCNF and CNF at various mass fractions.

cLSP and cLS was observed with unmodified CNF. cLSP and cLS with 20 wt.% of CNF displayed a stress of ≈16 and ≈10 MPa at the yield point, compared to ≈13 and ≈5 MPa when using the same content of TOCNF. The branched morphology of the unmodified CNF, as opposed to the more individualized TOCNF, leads to higher entanglement and interconnectivity around the particles, leading to higher cohesion. Overall, the cohesion is induced by CNF–CNF entanglement, but there is a significant contribution coming from particle-CNF secondary interactions. Lignin-based carbon particles are partially hydrophilic, thus being able to engage in multiple hydrogen bonding and van der Waals interactions with CNF.

Besides the higher cohesion, cLSP led to remarkably lower light reflectance, i.e., darker black, when compared to cLS (Figure 4c). When averaging the reflectance in the wavelength range from 300 to 800 nm, and comparing binder content and type, we observed a clear trend of increased light reflectance at higher binder contents, but there was no clear correlation with binder type. The effect of binder content on increasing the light reflectance was more pronounced for the cLS-based dried inks, which is due to the formation of thicker paper-like assemblies on the surface of the cLS particles (20–200 µm) as opposed to the loose (and more isolated) nanofiber network observed around the 900 nm cLSP.

TOCNF-based binding led to dried inks with slightly higher light reflectance when compared to unmodified CNF used at the same loading, with clear differences observed when using up to 9 wt.% binder. This is counterintuitive considering that the negative charge of TOCNF has been shown to induce high dispersibility of carbon nanomaterials,[22] as well as films that are more transparent than those of unmodified CNF.[23] The high dispersion of the cLSP/cLS carbon particles and smaller (more transparent) nanofiber binders were expected to lower the light reflectance; however, we observed that the combined factors resulted in better packing of the particle-nanofiber network and therefore denser structures (Table S2, Supporting Information). Pore morphology and content are important factors in the design of structural blackness. Membranes prepared from biobased black inks had a porosity over 40% and peaked at 54% for the ink precursor containing 9 wt.% of unmodified CNF and cLSP (Table S2, Supporting Information). The latter was, in fact, the bioink precursor leading to the blackest pigment (Figure 4e).

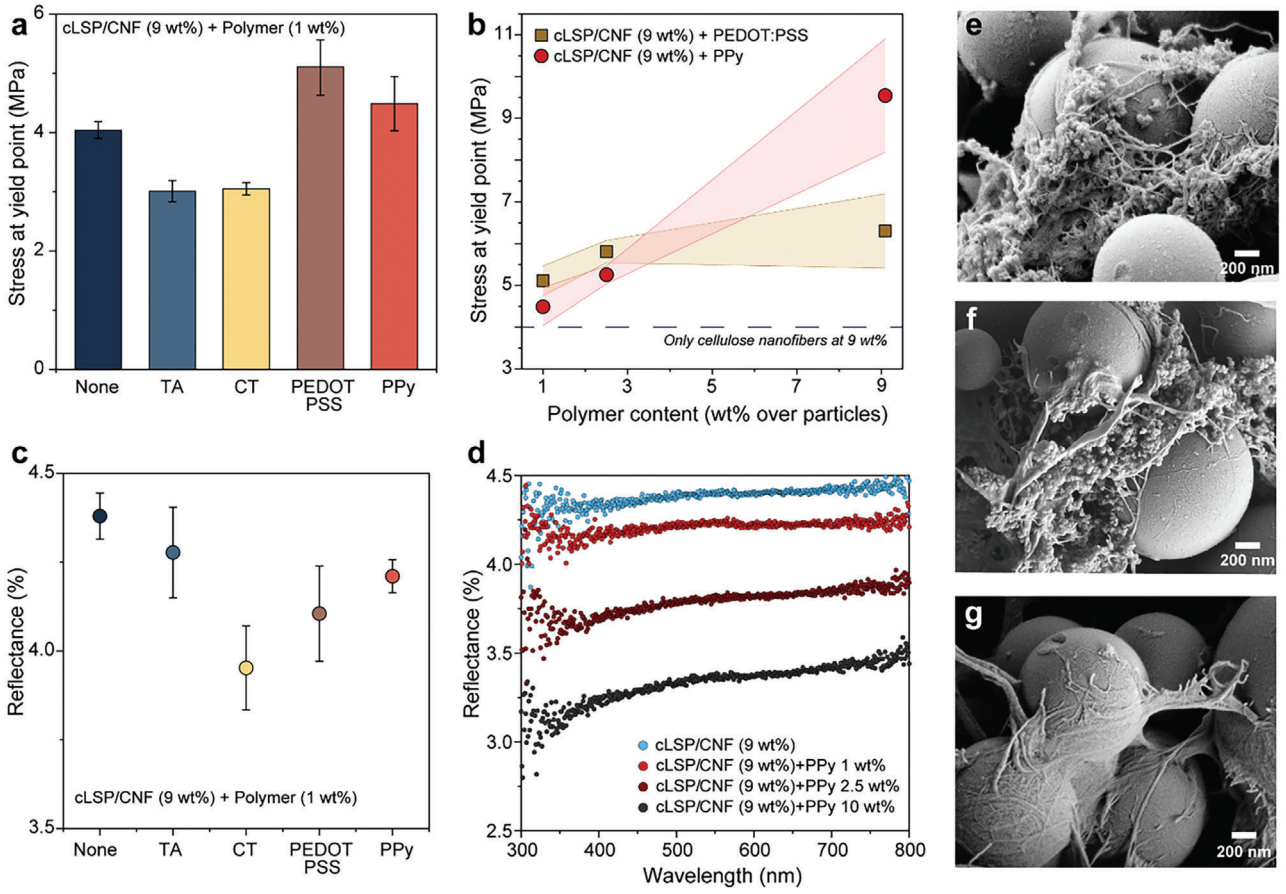

Figure 5. Cohesion and light reflectance properties of macroscopic constructs prepared from polymer-added black bioinks. a) Stress at yield point as a function of polymer additive (CNF 10% and polymer 15, related to the mass of black pigments), and b) stress at yield point for PPy and PEDOT:PSS at increased concentrations. c) Averaged reflectance (300–800 nm) of cLSP membranes consolidated with the addition of 1% of polymers, and d) reflectance spectra for materials containing 10% CNF and increased content of PPy. Scanning electron microscopy images of cLSP-CNF membranes (10% of binder) added of e) PPy, f) PEDOT:PSS, and g) CT, all at 10% related to the mass of particles.

Using superstructured inks, without additives, we obtained reflectance values of *ca.* 4% and 6.5% with cLSP and cLS, respectively. These values are significantly smaller than that of inks used in inkjet printing and fresh black inks, *ca.* 12% (Figure S6, Supporting Information). Moreover, although the blackness of the plant-based bioinks is not in the superblack levels, i.e., R% < 0.4, it is comparable to those of carbonized wood cross-sections (*ca.* 3%),[24] and it is lower than poly(lactic acid)-carbon black electro spun membranes.[25]

2.3. Effect of Polymeric Additive on the Performance of Black Bioinks

We investigated the effect of polymeric additive on the cohesion and light reflectance of dry inks. Both natural and synthetic polymers have been used to manage light interactions in materials. Tannic acid (TA) and condensed tannins (CT), i.e., plant-based polyphenols, have been incorporated in packaging materials to enable UV blocking properties[26–28] as well as to strengthen the material via crosslinking.[29] Moreover, polypyrrole (PPy) and poly(3,4-ethylenedioxythiophene) polystyrene sulfonate (PEDOT:PSS) have been used to assemble materials that are used to harness light in various WLs.[30–32] Herein, we fixed the CNF binder content at 10%, and varied the polymer fraction from 1% to 10% (both with respect to the mass of the cLSP black pigment).

The addition of TA and CT at 1% resulted in weaker materials when compared to those obtained with only CNF (**Figure 5**a). The strength of particle-nanofiber network is primarily associated with fibril–fibril interactions and, to a lesser extent, to fibril-particle interfacial coupling. The presence of macromolecules in the CNF binder suspension disrupted the cohesive fibril-fibril interactions due to the strong adsorption of tannins on the surface of cellulose.[28] The addition of PPy and PEDOT:PSS at the same fraction, however, led to stronger materials when compared to the reference CNF and tannin-added binder (Figure 5a). PPy and PEDOT:PSS are not soluble in water, and form stable dispersions in aqueous media (10–50 nm polymeric particles). Particles in this range could accommodate in the interstitial spaces of the network of cLSP black pigments, as well as co-assemble with cellulose nanofibers around the pigment particles (Figure 5e,f). Such

physical interactions do not disrupt cellulose fibril–fibril interactions and add to the cohesion due to the chemical compatibility of PPy/PEDOT:PSS with carbon particles. The mechanical strength of the PPy/PEDOT:PSS-containing inks increased with increased fractions of both polymers (Figure 5b), reaching over 9 MPa at the highest content, which is two times higher than that when only CNF is used. We emphasize that the CNF is the primary component bringing cohesion to the system, and the polymer additive boosts such cohesion. The polymer alone is not sufficient to create cohesive inks, to the extent that it is not possible to measure the strength. The strongest consolidated materials were originated by combining 1:1 CNF and polymer additive, both at 10% of the pigment mass fraction in the ink. The dry ink contained 83.3 wt.% of cLSP, 8.3 wt.% CNF, and 8.3% polymeric additive.

The addition of polymers with aromatic and conjugated features, which induce *HOMO-LUMO* transitions with low energy input, lowered further the overall reflectance of the consolidated black bioinks (Figure 5c,d). The condensed molecular structure of CT led to high absorption at short WLs (Figure S7, Supporting Information), leading to an overall low reflectance (Figure 5c). Tannic acid led to relatively higher absorption of WLs close to the UV range (Figure S7, Supporting Information), whereas PEDOT:PSS addition induced high scattering at the edges of the tested WLs (Figure S8, Supporting Information). This explains the high standard deviation after averaging the reflectance values obtained across the 300–800 nm WLs. PPy led to very consistent reflectance across the measured range, which, coupled to its high cohesion, makes it an ideal polymeric additive for black bioinks. Moreover, increasing the PPy content from 1% to 10% (based on the mass of black pigments), we observed a decreased light reflectance, from 4.2% to 3%. Higher content of PPy would not result in lower reflectance values (Figure S8, Supporting Information), therefore setting a lower limit for light reflectance at *ca*. 3% for the composited bioinks. This is not only related to chemical-derived blackness but also to new structural features introduced by the polymer (Figure 5e,f), which were absent in the tannin-added inks (Figure 5g). The presence of small nanoparticles between the submicron particles, and within the nanocellulose network, created a porosity with length scales <10 nm that enhanced multiple internal reflections, but also reduced the flatness of the top surface of the consolidated ink. Flat, featureless, surfaces are known to decrease light absorption due to the principles of (specular) light reflectance, i.e., $\theta_i = \theta_r$, where light reflects ($_r$) at the same angle (θ) of incidence ($_i$). Our consolidated inks are superstructures of particles-nanofibers (added polymers) with a multiscale architecture that is efficient to reduce the reflection up to four-fold when compared to commercial pigments (Figure S6, Supporting Information).

2.4. Compositional and Structuring Factors in Colloidal Bioinks

So far, we have demonstrated that colloidal inks result in dry porous constructs (schematically represented in **Figure 6**a) that display lower light reflectance when compared to monolithic (macroscale) black surfaces (Figure 4c). We experimentally assessed the optical properties of air-dried black surfaces generated by inks containing 900 nm lignin-based carbon pigments and nanocellulose binders. Next, we modeled the optical properties of randomly packed particles (of various sizes), to discuss the effect of pigment size and porosity (affected by the drying dynamics)[33] of the consolidated system on its light reflectance. Finite element (FE) software COMSOL Multiphysics (Electromagnetic Waves, Frequency Domain in Wave Optics Module), in the framework of continuum description of condensed matter, was used to model the optical properties of several particle constructs (Figure 6b and Figures S9–S15, Supporting Information). More details of the modeling framework are found in the Experimental Section and Section S2 (Supporting Information). The overall reflectance values obtained in the modeling are in a slightly higher regime that those observed experimentally. This discrepancy derives from the bulk porosity and optical properties of the model material (a graphite pellet, Section S2, Supporting Information), which may not match perfectly with those from the lignin-based carbon particles. Biobased carbon typically displays micro–meso porosity,[34,35] which may also contribute to decreasing the light reflectance.

Overall, in the modeled carbon-based particulate constructs—within the size range tested—the porosity played a bigger role in the averaged light reflectance (300–800 nm) (Figure 6c). Reflectance values decrease from *ca*. 15% to 6%, i.e., by a factor of *ca*. 2.5, when increasing the porosity of the model graphite from a nearly monolithic material to an aerogel-like structure displaying porosity over 80%.[36] The effect of porosity becomes evident in the finite element modeling maps of the distribution of the electric field norm for $\lambda = 300$ nm, obtained from a particle construct displaying porosities of 90% (top) and 50% (bottom) (Figure 6d). Higher porosity, within a given size of the primary building blocks, leads independently to a more open path for light to penetrate deeper into the light-absorbing carbon structure, thus intensifying multiple internal reflections (MIR) mechanism that increases the light-substrate interactions and reduces overall the outward reflection. In particle-based materials or coatings, the porosity can be adjusted by following different drying methods and controlling their dynamics. For instance, Cusola et al. have shown that the packing density of lignin particle coatings produced by evaporation induced self-assembly can be controlled by simply controlling the drying temperature (from 25 to 100 °C).[33] On the other hand, particle-based materials with porosity over 70% require more specialized techniques, such as freeze drying of foamed particle precursors.[37]

The particle size of the primary elements used in the model constructs, however, had a minor impact on their overall visible light reflectance. Although there is a remarkable difference between a flat, featureless graphitic surface when compared to surfaces of nano-micro particle assemblies (Figure 6f), there is not a significant difference among particles sizes (in the range of 5 µm to 200 nm) as far as the total light reflectance (Figure S15, Supporting Information). In fact, light reflectance is reduced when using particles in the upper submicron sizes (500–900 nm). Assemblies of submicron particles create interparticle spaces with length scales in the submicron regime as well, which enables light with wavelength in the visible range to penetrate the structure and promote MIR (Figure S11 and Figure S12, Supporting Information). Elementary particles in the range of 200 nm—especially in denser structures—tend to create

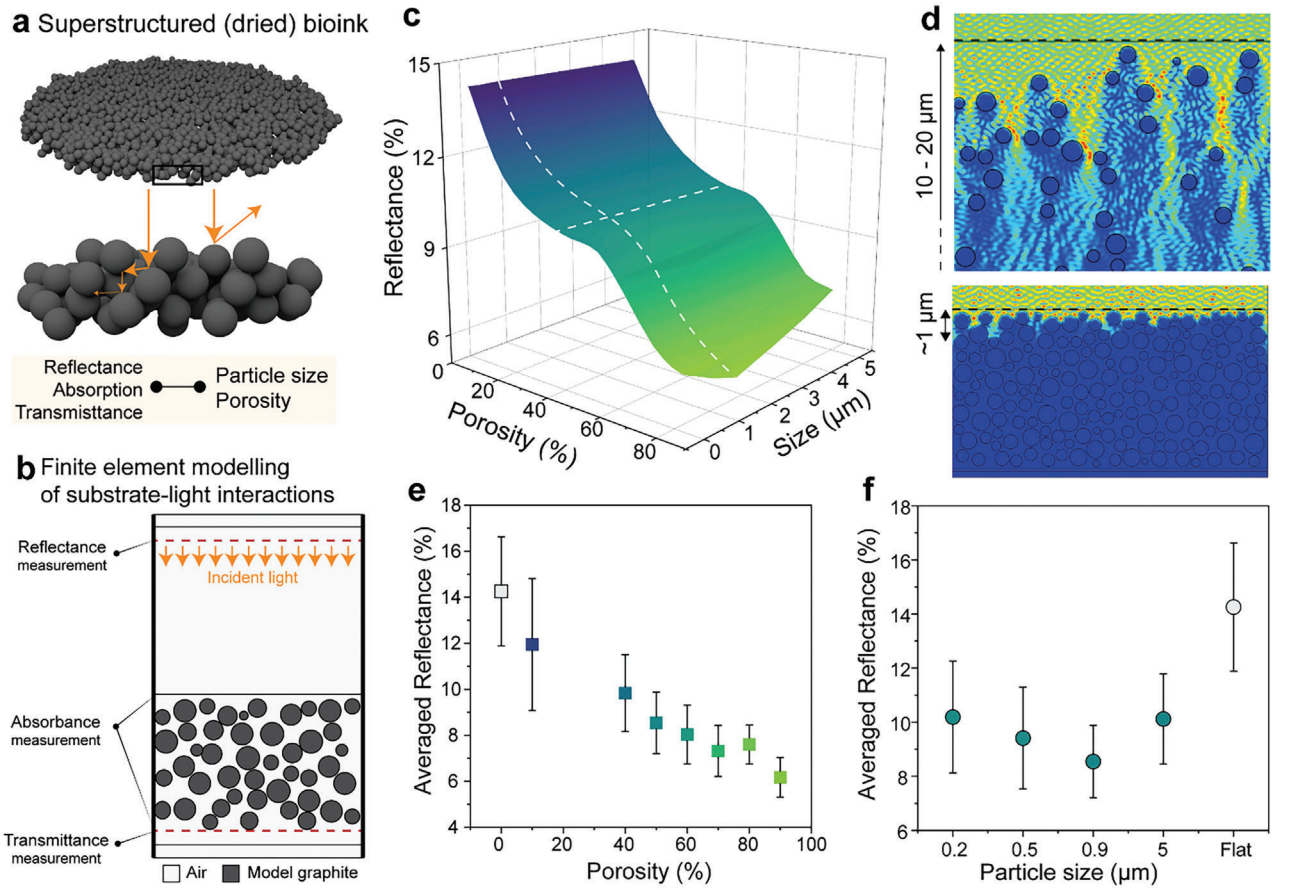

Figure 6. a) Schematic representation of the particulate construct obtained after the drying of the black bioinks. Substrate-light interactions are dominated by particle size and porosity. b) Simplified scheme (more details in Supporting Information) of the finite element modeling (FEM) of optical properties of particles beds used to further discuss the substrate light interactions taking place in consolidated black bioinks. c) 3D plot of modeled averaged light reflectance values as a function of porosity and particle size. d) Distribution maps of the electric field norm for $\lambda = 300$ nm, obtained from a particle construct displaying porosities of 90% (top) and 50% (bottom) and particle size of 0.5 µm. FEM results for averaged reflectance (300 to 800 nm) for particle constructs with e) increased porosity and f) various particles sizes.

tighter particle networks enabling substrate-light interaction mostly at their top surface (Figure S13, Supporting Information). Experimental measurements of the light reflectance of dried bioinks made from 200 nm lignin-based carbon particles and CNF, confirmed the FE simulation (Figure S16, Supporting Information). In constructs made from bigger particles (*ca.* 5–50 µm), their primary elements can already be considered as bulk, monolithic structures thus exposing hundreds of squared microns with low radii of curvature (Figure S10, Supporting Information) at the top surface (exposed to light) thus leading to light reflectance outward the coating or material.

2.5. Black Bioink Applications Prospects

The complex network of particles and nanofibers led to a light reflectance of *ca.* 3–4%, which is below the blackness found in most pigmentation-centered applications. Nevertheless, the use of nanocellulose as a structural binder enables adherence to a variety of surfaces, including polyester, paper, and wood (**Figure 7** and Figure S17, Supporting Information). This corroborates to the ability of cellulose nanomaterials to act as adhesive.[13,38] The ink adheres very strongly to the substrates, resisting several mechanical stresses related to folding, rolling, and crumpling without any apparent damage (Figure S18, Supporting Information). Given the hydrophilic character of the cellulosic binder, the current formulation should be sensitive to water, thus requiring further development or considerations on using existing water-resistant additives. The viscosity of the ink is controlled by the nanocellulose content (Figure S19, Supporting Information), which allows to match the required flow behavior of the application. The high aspect ratio of the binding nanofibers leads to shear thinning (Figure S19a, Supporting Information), whereas the interconnectivity of the CNF network results in elastic structures over a wide range of shear stresses (Figure S19b, Supporting Information). The viscosity of the black bioinks can be adjusted to cover a range over two orders of magnitude, within the same shear stress, by varying the binder content between 2–25% based on the carbon particle (i.e., pigment) mass fraction in the ink. Therefore, using the same components it is possible to produce low viscosity formulations for coatings (Figure 7a), writing (Figure 7b), stamping and processes such as casting

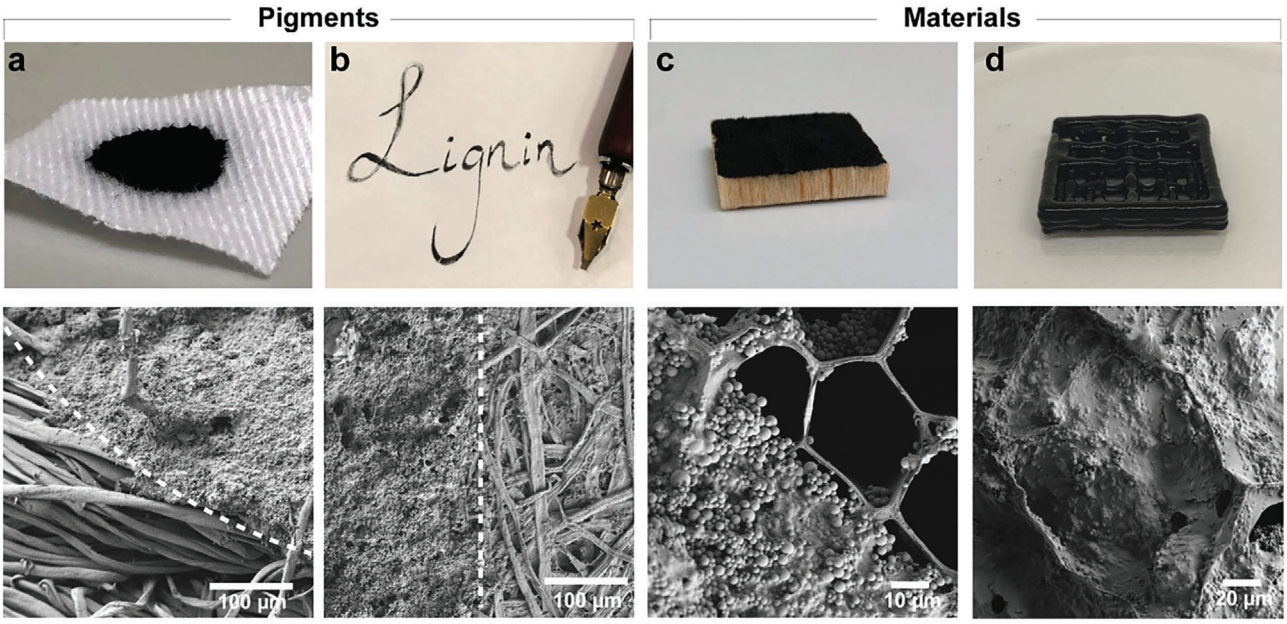

Figure 7. Demonstration of applications for black bioinks in pigments and as precursors for the fabrication of carbon materials. Plant-based black bioinks were used to a) coat polyester fabric, b) as inks in dipping pens, c) coat the cross section of wood to enable solar-powered stem generation, and d) 3D print scaffolds that can find several final applications.

(Figure 7c). Higher viscosity inks, i.e., with higher nanocellulose content, may find applications in brush painting, e.g. to gain control over thixotropic behavior of the ink.[39,40] Nevertheless, the shear thinning and elastic behavior (in a wide range of shear stress, Figure S19b, Supporting Information) of nanocelluloses make the black inks suitable for printing technologies, such as 3D printing (Figure 7d). 3D printing is facilitated by replacing the unmodified CNF by TOCNF, which are smaller in size and facilitates extrusion through the nozzles. This also applies to inkjet printing, where smaller carbon pigments (≈200 nm) should induce better printability of smaller droplets (pL volumes) and higher resolution of the printed pattern.

The black bioinks could be utilized as precursors for the development of several materials that rely on carbon properties, including carbon capture,[34] electrocatalysis,[41] filtration,[42] electromagnetic shielding,[43] and heat-induced solar steam generation.[44] Such wide variety of applications is a result of the versatility of our materials as far as formulation, and because the nanocellulose binder does not hinder access to the surface and functionality of the particles. As a demonstration, herein we coated a cross-section of balsa wood with a low viscosity black bioink (containing *ca.* 5 wt.% of nanocellulose). The darkened surface was then exposed to simulated sunlight while the bottom of the sample was immersed in water. We follow the evaporation rate (kg h^{-1} m^{-2}), and compared to a fully carbonized wood scaffold, a structure that has been often used for such purposes. In fact, the coated wood surface performed similarly to the fully carbonized material, 2.5 kg h^{-1} m^{-2} compared to 3 kg h^{-1} m^{-2} (Figure S20, Supporting Information) with the advantage of displaying the mechanical strength inherent to natural wood. This is not the case of carbonized wood—a very brittle material. Nevertheless, with the presence of either PPy or PEDOT:PSS (10% over the particle content) the consolidated ink was electrically conductive, which we demonstrated by creating a simple circuit on a wood veneer (Figure S21, Supporting Information).

3. Conclusion

We produced black bioinks using light-absorbing particles formed by lignin precursors and a "transparent" binder, namely, cellulose nanofibers. The cohesion of the particle-nanofiber networks, i.e., the dried bioinks, is easily tuned by the nanofiber loading (with only 10 wt.% nanocellulose addition a highly robust ink is produced). The blackness of the bioinks, which is higher than traditional fossil-based black pigments, is explained from the coupling of chemical and structural features. For instance, while the graphitic structure of the lignin black pigments enables light absorption in the visible range via low-energy *HOMO-LUMO* transitions, the particulated nature of the introduced constructs enables multiple internal reflections and light trapping, thus reducing the overall light reflectance. The configuration and structure of the particle-nanofiber network, especially its porosity, plays a major role in light reflection. We assessed the influence of morphology on the blackness of the substrate using finite element modeling of the optical properties of idealized particle beds.

The blackness of the bioinks could be lowered down with the addition of polymeric additives, such as PPy, but this must be rationalized in terms of performance-renewability. The purely plant-based bioinks display not only a high performance but are sustainable alternative to traditional black pigments, e.g., those based on fossil carbon or metals. Given their graphitic nature, the bioinks can be used in a variety of platforms (light energy and electroactive materials, among others). More specific and application-centered characterizations, e.g., thixotropic behavior, are required to further develop these black bioinks. The formulation and the tailorable rheology open additional opportunities in

the fabrication of carbon-based materials with a broad window of practical applicability.

4. Experimental Section

Materials: Ligninosulfonate (Ultrazine NA, Borregaard, Norway) was used as received. Polypyrrole (CAS: 30604-81-0), poly(3,4-ethylenedioxythiophene)-poly(styrenesulfonate), PEDOT:PSS (CAS: 155090-83-8), 2,2,6,6-tetramethylpiperidine-1-oxyl (TEMPO) (CAS: 2564-83-2), sodium bromide (NaBr, CAS: 7647-15-6), and sodium hypochlorite solution (NaClO, CAS: 7681-52-9) were purchased from Merck.

Synthesis of Spherical Particle of Lignin and the Carbonized Particles: The synthesis of spherical lignin particles was based on the previous reports.[21,45] Briefly, lignosulfonate (LS) was dissolved in water and fed to a spray dryer unit (ADL311S-A, Yamato Co., Ltd. Japan) for the synthesis of the spherical particles from 3% lignin/water solution. The unit included a two-fluid nozzle atomizer, a heated reactor, and a cyclone collector. The processing temperature was set to 100 °C, atomizing pressure of 0.13 MPa and flow rate of 0.44 L min^{-1}. The original lignosulfonate powder and the synthesized spherical lignin particles were thereafter denoted as LS and LSP, respectively. The LSP was then carbonized in a tube furnace under nitrogen flow. The temperature was increased from room temperature to 600, 700, 800, and 900 °C at 2 °C min^{-1} and held at isothermal conditions for 2 h. After carbonization, the samples were washed with hot water followed by ethanol to remove soluble pyrolysis residues and then vacuum dried at 80 °C.

Preparation of Nanocelluloses: Never-dried bleached kraft birch pulp (BKBP) was diluted to 1% (w/v) in deionized water. The fibers were first processed in a high-shear homogenizer for 5 min at 10 000 RPM (T18 ULTRA-TURRAX – IKA) and then fibrillated into cellulose fibrils (CNF) using a high-pressure microfluidizer (Microfluidics M110P) operating with one pass through 400 to 200 µm chamber followed with six passes in a 200 to 100 µm chamber at 2000 bar. TEMPO-mediated oxidized cellulose nanofibrils (TOCNF) were produced following the method described by Saito et al.[46,47] Briefly, BKBP fibers were suspended in water containing an equivalent of 0.13 mmol TEMPO and 4.65 mmol NaBr. Then, the NaClO solution (at 3.5 mmol g^{-1} of cellulose) was added to the fibers to initiate the oxidation, which occurred over 2 h. The oxidized fibers were washed and homogenized in a microfluidizer (Microfluidics M110P) using one pass through 200 to 100 µm chamber at 2000 bar. The carboxylic groups were quantified by conductometric titration according to standard SCAN-CM 65:0278, which indicated a charge of 1.3 ± 0.05 $mmol_{COOH}/g_{fiber}$.

Preparation of the Black Bioinks: Nanocellulose suspensions were diluted to 0.4% (w/v) and homogenized in bath ultrasonication for 30 min. Then, varied contents of particles were added to the suspensions aiming at a nanocellulose percentage related to the mass of particles of 2%, 5%, 10%, and 25%. This resulted in final nanocellulose content of 1.9, 4.7, 9, and 21 wt.% of the total solid content of the inks. The particle-nanocellulose mixtures were vortexed for 1 min, followed by bath ultrasonication for 5 min. This was repeated until a homogenous mixture was obtained (after *ca*. five times). In the polymer-containing inks, given masses of polymer (with contents ranging from 1% to 10% related to mass of particles) were added to the nanocellulose suspensions before the addition of particles. The following mixing steps were kept the same.

Rheology: The apparent viscosity was measured using a rheometer (MCR 302, Anton Paar, Germany) equipped with parallel plates (PP25) and a gap fixed at 1 mm. The shear viscosity was monitored at varying shear rates (0.01 to 100 s^{-1}). The linear viscoelastic regime was determined with an amplitude sweep (0.01% to 100%) at a fixed frequency of 10 rad s^{-1}. Storage (G') and loss (G'') moduli were obtained as a function of amplitude, and the yield point was taken into account for the 3D printing demonstration. All measurements were performed at 23 °C. The use of a covered parallel plate edge was noted by using silica oil, which prevented sample evaporation during the tests.

Consolidation of the Bioinks for Mechanical, Reflectance, and Morphology Characterizations: Polydimethylsiloxane (PDMS) molds were fabricated and used as templates for the assembly of cylinders and discs from the aqueous black bioinks (Figure S18, Supporting Information). Then, for the assembly of cylinders, 50 µL of the black bioinks were cast in a PTFE hydrophobized PDMS mold[48] and allowed to dry in air. The obtained cylinders were used to evaluate the mechanical cohesion of the dried inks by uniaxial compression. To evaluate the light reflectance of the dried inks, 9 mm wide discs were assembled by casting 200 µL of the bioinks in a UV treated glass mounted with the PDMS restrainer (Figure S22, Supporting Information) and allowing the cast ink to dry in air.

Mechanical Characterization: The mechanical strength of the foams was evaluated by uniaxial compression using a TA.XTplusC Texture Analyzer. The measurements were carried out at a compression rate of 0.10 mm s^{-1} and within a conditioned environment (23 °C and 50% RH).

UV–Vis Spectroscopy on Reflectance Mode: UV–vis spectra, in the range of 300 to 800 nm, were acquired using a Cary 5000 (Agilent, USA) spectrophotometer. The total reflectance of the dried bioinks was measured in air using an integrating sphere (DRA 2500, Agilent).

Imaging by Scanning Electron Microscopy (SEM): Field-emission SEM was carried out in a Zeiss Sigma (VP, Germany) using an acceleration voltage of 2 kV. The samples were coated with a 4 nm thick platinum/palladium layer on a Leica EM ACE600 high vacuum sputter coater.

X-ray Tomography: The $cLSP_{(CNF)}$ and $cLS_{(CNF)}$ materials were imaged with Xradia MicroXCT-400 device with 1.15 µm pixel size. X-ray source voltage and power were set to 40 kV and 4 W, respectively. Total of 1861 projection images over 180° angular range (+ cone angle) were acquired with 15 s exposure time per image. The projections were reconstructed into volume images using the pi2 software (available at github.com/arttumiettinen/pi2). To better visualize the structure of the material containing smaller lignin particles, the $cLSP_{(CNF)}$ sample was imaged also with Xradia NanoXCT-100 tomograph with 65 nm pixel size. In this case, monochromatic X-rays corresponding to copper Kα-peak were used to expose 1081 projections with 150 s exposure time each, over 180° angular range. The projections were aligned and reconstructed into a volume image using software provided by the device manufacturer. The volume images were visualized with Fiji[49] and MeVisLab (available at www.mevislab.de) software packages.

The roughness of both surfaces of the $cLSP_{(CNF)}$ and $cLS_{(CNF)}$ materials were measured from the X-ray tomographic images. To this end, the surfaces of the material were determined using the "Carpet" algorithm[50] that finds the interface between the inside and the outside of the materials as the converged position of a moving (imaginary) surface that follows specific Edwards–Wilkinson dynamics. This approach allows defining the material surface despite roughness and deep cavities often occurring in a fiber network. The resulting surface height maps were high-pass filtered (= 200 µm) such that surface height variations resulting from global curvature of the sheets were eliminated. Finally, the height maps were used to find surface height distribution, mean height Sa, and RMS height Sq. The image analysis was conducted with the pi2 software (available at github.com/arttumiettinen/pi2).

FE Modeling with COMSOL Multiphysics: In the framework of continuum description of condensed matter, FE software COMSOL Multiphysics (Electromagnetic Waves, Frequency Domain in Wave Optics Module) was used for modeling the optical properties of randomly organized particles (of various sizes) beds. In 2D, the particles were modeled as circles randomly (uniformly) distributed throughout the computational domain. The particles sizes were generated with a normal distribution within given diameter ranges. For different porosity values, four model cases corresponding to particles were considered with mean diameter values of 5, 0.9, 0.5, and 0.2 µm. Material model used for the carbonized particles had wavelength-dependent real and imaginary parts of refractive index (corresponding to graphite pellet material). Optical properties of nanocellulose-based binder were assumed, for simplicity, to be close to air had real refractive index with value one. Sizes of the computational domains were taken to be sufficient for representing a statistically significant subset of the particle beds (and being at reasonable computational cost level). Incident light (with zero incidence angle) was modeled via Port boundary condition launching a plane (electric field) wave with wavelength values in a range from 300 to 800 nm. As particles reflect (and transmit) light

in random directions, Floquet periodic boundary conditions were used on the vertical sides of the modeling domain. Quadratic discretization was used for electric field. More details can be found in Section S2 (Supporting Information).

Supporting Information

Supporting Information is available from the Wiley Online Library or from the author.

Acknowledgements

The authors acknowledge funding support from the European Research Council (ERC) under the European Union's Horizon 2020 research and innovation program (grant agreement no. 788489, "BioElCell"), the Canada Excellence Research Chair Program (CERC-2018-00006). This work was a part of the Academy of Finland's Flagship Programme under Project No. 318890 and 318891 (Competence Center for Materials Bioeconomy, FinnCERES.

Conflict of Interest

The authors declare no conflict of interest.

Data Availability Statement

The data that support the findings of this study are available from the corresponding author upon reasonable request.

Keywords

carbonization, carbon materials, cellulose nanofibers, coatings, particle networks, pigments

Received: May 3, 2023
Revised: June 10, 2023
Published online:

[1] A. C. Ferrari, J. Robertson, *Phys. Rev. B* **2000**, *61*, 14095.
[2] Y. Xu, Q. Chu, D. Chen, A. Fuentes, *Front. Mech. Eng.* **2021**, *7*, 744001.
[3] A. Coccato, J. Jehlicka, L. Moens, P. Vandenabeele, *J. Raman Spectrosc.* **2015**, *46*, 1003.
[4] G. Pfaff, *Phys Sci. Rev.* **2021**, *7*, 109.
[5] C. G. Otoni, H. M. C. Azeredo, B. D. Mattos, M. Beaumont, D. Correa, O. J. Rojas, *Adv. Mater.* **2021**, *33*, 2170342.
[6] A. Bengtsson, P. Hecht, J. Sommertune, M. Ek, M. Sedin, E. Sjöholm, *ACS Sustainable Chem. Eng.* **2020**, *8*, 6826.
[7] W. Sun, A. Du, Y. Feng, J. Shen, S. Huang, J. Tang, B. Zhou, *ACS Nano* **2016**, *10*, 9123.
[8] D. E. McCoy, V. E. McCoy, N. K. Mandsberg, A. V. Shneidman, J. Aizenberg, R. O. Prum, D. Haig, *Proc. R. Soc. Edinburgh, Sect. B: Biol. Sci.* **2019**, *286*, 20190589.
[9] C. Tu, W. Cai, X. Chen, X. Ouyang, H. Zhang, Z. Zhang, *Small* **2019**, *15*, 1902070.
[10] J. Guo, D. Li, H. Zhao, W. Zou, Z. Yang, Z. Qian, S. Yang, M. Yang, N. Zhao, J. Xu, *ACS Appl. Mater. Interfaces* **2019**, *11*, 15945.
[11] Z. Yin, H. Wang, M. Jian, Y. Li, K. Xia, M. Zhang, C. Wang, Q. Wang, M. Ma, Q. S. Zheng, Y. Zhang, *ACS Appl. Mater. Interfaces* **2017**, *9*, 28596.
[12] Y. Kuang, C. Chen, S. He, E. M. Hitz, Y. Wang, W. Gan, R. Mi, L. Hu, *Adv. Mater.* **2019**, *31*, 1900498.
[13] B. D. Mattos, B. L. Tardy, L. G. Greca, T. Kämäräinen, W. Xiang, O. Cusola, W. L. E. Magalhães, O. J. Rojas, *Sci. Adv.* **2020**, *6*, eaaz7328.
[14] M. Österberg, M. H. Sipponen, B. D. Mattos, O. J. Rojas, *Green Chem.* **2020**, *22*, 2712.
[15] S. Yoshioka, Y. Takeoka, *ChemPhysChem* **2014**, *15*, 2209.
[16] B. D. Mattos, L. G. Greca, B. L. Tardy, W. L. E. Magalhães, O. J. Rojas, *Small* **2018**, *14*, 1801256.
[17] S. Sultan, H. N. Abdelhamid, X. Zou, A. P. Mathew, *Adv. Funct. Mater.* **2019**, *29*, 1805372.
[18] G. Zhou, M.-C. Li, C. Liu, Q. Wu, C. Mei, *Adv. Funct. Mater.* **2022**, *32*, 2109593.
[19] G. Zhou, M.-C. Li, C. Liu, C. Liu, Z. Li, C. Mei, *Adv. Sci.* **2023**, *10*, 2206320.
[20] T. Kim, C. Bao, M. Hausmann, G. Siqueira, T. Zimmermann, W. S. Kim, *Adv. Electron. Mater.* **2019**, *5*, 1800778.
[21] M. Ago, S. Huan, M. Borghei, J. Raula, E. I. Kauppinen, O. J. Rojas, *ACS Appl. Mater. Interfaces* **2016**, *8*, 23302.
[22] A. Hajian, S. B. Lindström, T. Pettersson, M. M. Hamedi, L. Wågberg, *Nano Lett.* **2017**, *17*, 1439.
[23] J. J. Kaschuk, Y. Al Haj, O. J. Rojas, K. Miettunen, T. Abitbol, J. Vapaavuori, *Adv. Mater.* **2022**, *34*, 2104473.
[24] S. He, C. Chen, Y. Kuang, R. Mi, Y. Liu, Y. Pei, W. Kong, W. Gan, H. Xie, E. Hitz, C. Jia, X. Chen, A. Gong, J. Liao, J. Li, Z. J. Ren, B. Yang, S. Das, L. Hu, *Energy Environ. Sci.* **2019**, *12*, 1558.
[25] Q. Ding, C. Guan, H. Li, M. Shi, W. Yang, H. Yan, X. Zuo, Y. An, S. Ramakrishna, P. Mohankumar, F. Zhang, *Sol. Energy* **2020**, *195*, 636.
[26] X. Huang, Y. Ji, L. Guo, Q. Xu, L. Jin, Y. Fu, Y. Wang, *Ind. Crops Prod.* **2022**, *180*, 114710.
[27] A. L. Missio, B. D. Mattos, D. de, F. Ferreira, W. L. E. Magalhães, D. A. Bertuol, D. A. Gatto, A. Petutschnigg, G. Tondi, *J. Cleaner Prod.* **2018**, *184*, 143.
[28] A. L. Missio, B. D. Mattos, C. G. Otoni, M. Gentil, R. Coldebella, A. Khakalo, D. A. Gatto, O. J. Rojas, *Biomacromolecules* **2020**, *21*, 1865.
[29] M. L. Picchio, Y. G. Linck, G. A. Monti, L. M. Gugliotta, R. J. Minari, C. I. Alvarez Igarzabal, *Food Hydrocolloids* **2018**, *84*, 424.
[30] W. Li, Z. Li, K. Bertelsmann, D. E. Fan, *Adv. Mater.* **2019**, *31*, 1900720.
[31] Y. Huo, D. Guo, J. Yang, Y. Chang, B. Wang, C. Mu, J. Xiang, A. Nie, K. Zhai, T. Xue, F. Wen, *ACS Appl. Electron. Mater.* **2022**, *4*, 2552.
[32] Z. Hanif, M. Z. Tariq, Z. A. Khan, M. La, D. Choi, S. J. Park, *Carbohydr. Polym.* **2022**, *292*, 119701.
[33] O. Cusola, S. Kivistö, S. Vierros, P. Batys, M. Ago, B. L. Tardy, L. G. Greca, M. B. Roncero, M. Sammalkorpi, O. J. Rojas, *Langmuir* **2018**, *34*, 5759.
[34] B. Zhao, M. Borghei, T. Zou, L. Wang, L.-S. Johansson, J. Majoinen, M. H. Sipponen, M. Österberg, B. D. Mattos, O. J. Rojas, *ACS Nano* **2021**, *15*, 6774.
[35] Y. Meng, C. I. Contescu, P. Liu, S. Wang, S.-H. Lee, J. Guo, T. M. Young, *Wood Sci. Technol.* **2021**, *55*, 587.
[36] J. Zhu, X. Yang, Z. Fu, C. Wang, W. Wu, L. Zhang, *J. Porous Mater.* **2016**, *23*, 1217.
[37] R. Abidnejad, M. Beaumont, B. L. Tardy, B. D. Mattos, O. J. Rojas, *ACS Nano* **2021**, *15*, 19712.
[38] B. L. Tardy, J. J. Richardson, L. G. Greca, J. Guo, H. Ejima, O. J. Rojas, *Adv. Mater.* **2020**, *32*, 1906886.
[39] H. Utsunomiya, Y. Tsujita, T. Kondo, *Cellulose* **2022**, *29*, 2899.
[40] A. Naderi, T. Lindström, J. Sundström, *Cellulose* **2014**, *21*, 1561.
[41] J. Wang, H. Kong, J. Zhang, Y. Hao, Z. Shao, F. Ciucci, *Prog. Mater. Sci.* **2021**, *116*, 100717.

[42] Z. Han, X. Xiao, H. Qu, M. Hu, C. Au, A. Nashalian, X. Xiao, Y. Wang, L. Yang, F. Jia, T. Wang, Z. Ye, P. Servati, L. Huang, Z. Zhu, J. Tang, J. Chen, *ACS Appl. Mater. Interfaces* **2022**, *14*, 1850.
[43] R. Kumar, S. Sahoo, E. Joanni, R. K. Singh, W. K. Tan, K. K. Kar, A. Matsuda, *Carbon* **2021**, *177*, 304.
[44] Y. Dong, Y. Tan, K. Wang, Y. Cai, J. Li, C. Sonne, C. Li, *Water Res.* **2022**, *223*, 119011.
[45] M. Suzuki, A. Kondor, Y. Sakuraba, O. J. Rojas, M. Ago, *Cellulose* **2022**, *29*, 2961.
[46] T. Saito, S. Kimura, Y. Nishiyama, A. Isogai, *Biomacromolecules* **2007**, *8*, 2485.
[47] T. Saito, I. Shibata, A. Isogai, N. Suguri, N. Sumikawa, *Carbohydr. Polym.* **2005**, *61*, 414.
[48] L. G. Greca, M. Rafiee, A. Karakoç, J. Lehtonen, B. D. Mattos, B. L. Tardy, O. J. Rojas, *ACS Nano* **2020**, *14*, 12929.
[49] J. Schindelin, I. Arganda-Carreras, E. Frise, V. Kaynig, M. Longair, T. Pietzsch, S. Preibisch, C. Rueden, S. Saalfeld, B. Schmid, J.-Y. Tinevez, D. J. White, V. Hartenstein, K. Eliceiri, P. Tomancak, A. Cardona, *Nat. Methods* **2012**, *9*, 676.
[50] T. Turpeinen, M. Myllys, P. Kekäläinen, J. Timonen, *IEEE Trans. Image Process.* **2015**, *24*, 5696.